Journal of Applied Geophysics 155 (2018) 162–175

Contents lists available at ScienceDirect

Journal of Applied Geophysics

journal homepage: www.elsevier.com/locate/jappgeo

Could magnetic properties be used to image a grouted rock volume?

R.J. Lunn [a,*], L.T. Corson [a], C. Howell [a], G. El Mountassir [a], C. Reid [a], S.L. Harley [b]

[a] Department of Civil & Environmental Engineering, University of Strathclyde, 75 Montrose St, Glasgow G1 1XJ, United Kingdom
[b] School of Geosciences, Grant Institute, The King's Buildings, James Hutton Road, Edinburgh EH9 3FE, United Kingdom

ARTICLE INFO

Article history:
Received 21 December 2017
Received in revised form 14 June 2018
Accepted 17 June 2018
Available online 19 June 2018

Keywords:
Ground engineering
Detectable grout
Geophysical monitoring
Rock grouting
Numerical modelling
Magnetic field detection

ABSTRACT

In this study, we show that development of a detectable permeation grouting system is feasible, based on the addition of magnetic materials to the grout, specifically, magnetite. A magnetic-based detection system is selected for development because unlike other previously trialled detection methods, magnetic fields are detectable over large distances within the subsurface, and importantly, attenuation of the magnetic field is not strongly dependent on the material properties of the surrounding rock. To test the conceptual feasibility of such a system, a finite element based numerical model is developed to simulate the magnetic field anomaly that can be achieved by the addition of magnetic materials to a cement grout. The model is verified against an analytical solution and then used to predict the magnetic field generated by a grouted cylinder of rock, assuming a fixed percentage of uniformly distributed magnetic minerals, and a central injection borehole. Two field trials are conducted to verify the detectable grouting concept, the first using a walkover survey that allowed mapping of the magnetic signal in 2D. The second is designed to mimic magnetic field measurements from a borehole monitoring array, with a single central magnetic grout block (representing the grout close to the injection point). Results of the two field trials show that the magnetic cement is detectable, even when the background magnetic noise within the surrounding soils/rocks is significant. A good agreement is obtained between the measured and the modelled magnetic anomaly. This research opens the door to the development of a 'detectable' magnetic grouting system, that can increase confidence in the integrity of grouted rock volumes and reduce the inefficiencies currently present in the grouting industry, enabling in-situ real-time optimisation of grouting campaigns.

1. Introduction

Cement grouting of rocks is widely used for reducing the hydraulic conductivity of underground structures (Li et al., 2016), of founding layers below dams and their interface with the dam core (e.g. Rastegarnia et al., 2017), for hydraulic containment of underground storage and disposal sites (e.g. Tsuda et al., 2012) and for the filling of underground shafts and cavities prior to construction of major infrastructure (Meier and Hoffmann, 1999). The most popular method within Europe for design and control of grouting campaigns is the empirical Grouting Intensity Number (GIN) method (Lombardi, 1996; Brantberger et al., 2000). The GIN method combines observations of pressure and injected volume to calculate a grouting intensity number. When kept below a user defined threshold, the GIN controls the energy applied to the fractures, thus avoiding fracture jacking and uplift. El Tani (2012) reformulated both the GIN and North American grout refusal criteria to calculate grout penetration based on an analytical model of radial flow of a Bingham fluid into a planar fracture. However Rafi and Stille (2015) demonstrated via a case study that the GIN value should be defined based on knowledge of grout spread, particularly for fractures at shallow depths or fractures requiring a high level of sealing. They presented an analytical solution for estimating grout penetration that includes the deformation of fractures during grouting.

The common assumption in the control of all permeation grouting campaigns is that grout penetrates radially from an injection borehole. This assumption is necessary, but invalid; in a rock with varying fracture apertures, individual fractures cross-cutting the injection borehole will have varying principal grout flow directions and variable penetration distances. The need to assume radial flow derives from an inability to detect the extent of grout penetration during and after injection. The definition of the GIN value without knowledge of grout penetration can result in the application of overly high injection pressures, with the result that grout penetrates beyond the target zone (waste of grout material), and unwanted uplifting occurs. On the other hand too low injection pressures can result in incomplete filling, with the result that grouting campaigns tend to be overly conservative relying on split-spacing boreholes. This results in grout wastage, drilling of unnecessary boreholes and a lack of data for true design optimization. In some circumstances, gaps in grout curtains may remain unknown. This is of

* Corresponding author.
E-mail address: rebecca.lunn@strath.ac.uk (R.J. Lunn).

https://doi.org/10.1016/j.jappgeo.2018.06.015

particular concern where hydraulic containment is critical. Without knowledge of grout penetration it is not possible to optimize design of the grout injection.

Several methods for detecting grout penetration have been previously proposed within the research literature; all have significant drawbacks and none are widely used within the construction industry. Chen et al. (2000) added fluorescent particles to grout to visualise grout spread. However, this is an intrusive approach which required penetration of the grouted rock using inspection boreholes and a downhole television logging system. This approach would ultimately compromise the integrity of a grout curtain by the drilling of inspection boreholes in the grouted rock volume. Majer (1989) proposed that high frequency seismic monitoring could be used a potential real-time monitoring system of grout penetration. However, the author was unable to correlate the location of the grout with the seismic activity recorded, in fact, the only seismic events that could be located occurred after the injection of grout had ceased. Ground penetrating radar has also been investigated as a potential method for the detection of different grouts behind tunnel linings (Zhang et al., 2010). However grout was only detected at distances less than 1 m and not in the presence of utilities within the tunnel. Detection of GPR signals is only expected to be possible over several meters as the signal is strongly attenuated by the ground. Furthermore detailed knowledge of the electrical properties of the material at the particular site where monitoring is to take place would be required. pH monitoring was used to infer grout spread in the design of the grouting campaign at Dounreay (UK) to hydraulically isolate a vertical shaft containing nuclear waste (Henderson et al., 2008). Grout penetration distances were estimated using the pH as an indication of grout breakthrough (Henderson et al., 2008) with some success. However, relying on pH measurements has drawbacks: it is not possible to locate the penetration front of the grout itself (as bleed water in advance of the grout front also exhibits a high pH) and it is generally not permissible for invasive observation boreholes to be located within the rock volume that is to be grouted.

In this paper, we test the feasibility of a new approach to detect grout penetration, through the addition, and subsequent detection, of magnetic minerals to cement grout. We develop a numerical model to demonstrate the feasibility of a magnetically detectable grouting system and compare our model with the results from two surface-based field trials. The key objectives of this study are to determine whether, and over what distance, cement grout containing magnetite particles is detectable in the subsurface, and whether different shaped magnetic grout blocks (volumes) produce detectably different magnetic fields.

2. Theoretical concept

To-date, no researchers have investigated the use of magnetic properties for grout detection. When compared to other geophysical approaches, a magnetic-based detection system could have significant advantages: (1) magnetic materials can be detected over large distances within the subsurface, (2) attenuation of the magnetic signal strength is not dependent on the properties of the surrounding material (i.e. rock, water or air), and (3) at any one location, the magnitude and direction of a magnetic field generated by a magnetic body is dependent on the shape and location of the magnetic body. Hence, theoretically, the shape and location of an injected magnetic grout within the ground may be accurately determined without requiring a priori knowledge of the in-situ rock/soil properties.

To determine the theoretical feasibility of developing a magnetically detectable grout, a numerical model was developed to simulate the 3D magnetic field produced by a known volume of magnetic material within the ground, subject to the Earth's magnetic field. There are many different types of magnetic materials; their magnetic properties differ based on their composition and crystal structure, and in the response of their electrons to an externally-applied magnetic field. Amongst naturally occurring magnetic minerals, magnetite (Fe_3O_4) has the largest magnetic susceptibility (up to $\chi = 650$) and the strongest remnant magnetization (up to 5000 A m^{-1}) (Kletetschka et al., 2000). Therefore, in the presence of an external magnetic field, such as that produced by the Earth, magnetite can produce a large magnetic anomaly.

2.1. Theoretical model

To model the magnetic field produced by the presence of a body containing magnetite within the ground, we use Maxwell's magnetostatic equations with the assumption that the region of interest is current free (Griffiths, 1999):

$$\nabla \times \mathbf{H} = 0 \tag{1}$$

$$\nabla \cdot \mathbf{B} = 0 \tag{2}$$

Here, $\mathbf{H}$ is the magnetic field (units: A m^{-1}), and $\mathbf{B}$ is the magnetic flux density (units: T). From Eq. (1), a scalar magnetic potential ψ can be defined such that

$$\mathbf{H} = -\nabla\psi \tag{3}$$

and hence we are only required to solve Eq. (2). The magnetic field $\mathbf{H}$ and the magnetic flux density $\mathbf{B}$ are related via the constitutive equation

$$\mathrm{B} = \mu\mathbf{H} + \mathbf{B}_r \tag{4}$$

where μ is the magnetic permeability and $\mathbf{B}_r$ is the remanent magnetic flux density. The magnetic permeability can be written as $\mu = \mu_0(1 + \chi)$, where $\mu_0 = 4\pi \times 10^{-7}$ NA^{-2} is the permeability of free space, and χ is the magnetic susceptibility of the magnetic body.

The total magnetic field can be split into a background field, $\mathbf{H}_b$, and an anomalous part, $-\nabla\psi_a$, that represents the magnetic field which arises from the presence of the magnetic body, such that $\mathbf{H} = \mathbf{H}_\mathrm{b} - \nabla\psi_a$. Eq. (2) then becomes

$$\nabla \cdot (\mu(\mathbf{H}_b - \nabla\psi_a) + \mathbf{B}_r) = 0 \tag{5}$$

This equation represents the governing equation for determining the magnetic field due to a body of magnetically-susceptible material within the Earth's magnetic field. To solve this equation for ψ_a, appropriate boundary conditions must be defined. On the boundary of the magnetic material, continuity of the magnetic field and continuity of the normal component of the magnetic flux density can be assumed, i.e.

$$[\psi_a]_1^2 = 0 \tag{6}$$

$$[\mathbf{n}\cdot\mathbf{B}]_1^2 = 0 \tag{7}$$

where the notation $[\ ]_1^2 = [\ ]_2 - [\ ]_1$ is used for the difference in a quantity across the boundary, and $\mathbf{n}$ is the outward unit normal of the magnetic body. On the exterior boundaries of the model, we impose

$$\psi_a = 0 \tag{8}$$

i.e. the field induced due to the presence of the magnetic grout is set to zero. This is a valid assumption if the boundaries are sufficiently far away.

A numerical model was developed to solve Eq. (5) with boundary conditions (6)–(8) within the finite element software platform, FreeFem++ (Hecht, 2012). After solving, the magnetic anomaly is given by

$$B_a = |\mu(\mathbf{H}_b - \nabla\psi_a) + \mathbf{B}_r| - |\mu\mathbf{H}_b| \tag{9}$$

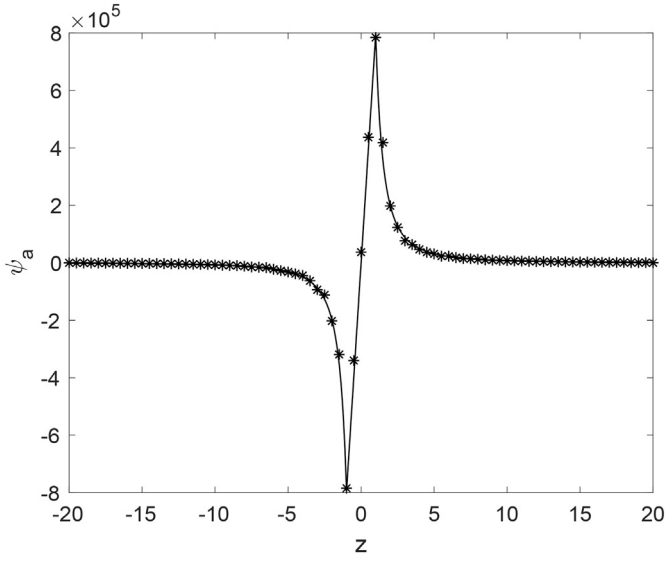

Fig. 1. Comparison of the analytical (solid line) with the numerical solution (asterisks) along the z-axis for a sphere with uniform permanent magnetisation.

which represents the magnitude of the anomalous magnetic field resulting from a magnetic body subjected to an external geomagnetic field.

2.2. Model verification

To verify the numerical model, the numerical and analytical solutions for a sphere with uniform permanent magnetisation in an infinite domain were compared. Taking $\mathbf{H}_b = \mathbf{0}$, $\chi = 0$, and $\mathbf{B}_r = B_{r0}\mathbf{e}_z$ inside the sphere and $\mathbf{B}_r = \mathbf{0}$ outside the sphere, where $\mathbf{e}_z$ is the unit normal in the z-direction, the magnetic scalar potential for a sphere of radius R is given by Griffiths (1999):

$$\psi_a = \begin{cases} \dfrac{B_{r0}}{3\mu_0} z & \text{inside sphere} \\ \dfrac{B_{r0}R^3}{3\mu_0} \dfrac{z}{(x^2+z^2)^{\frac{3}{2}}} & \text{outside sphere} \end{cases} \tag{10}$$

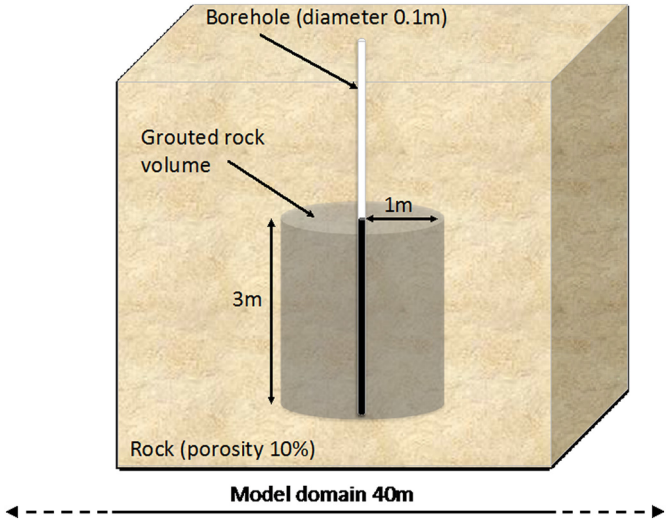

Fig. 2. Model schematic of grouted rock cylinder with central injection borehole.

Fig. 1 compares the analytical solution (solid line) with the numerical solution (asterisks) along the z-axis with $B_{r0} = 3$ and $R = 1$. There is excellent agreement between both solutions.

2.3. Feasibility of magnetically detectable grout

Once verified, the numerical model can be used to determine the feasibility of a magnetically detectable grout. Simulations were performed to predict the magnetic field generated by a grouted cylinder of rock with a central injection borehole (see Fig. 2). The cylinder was of length 3 m with a borehole radius of 0.05 m. A total radius of grout penetration of 1 m and a rock porosity of 0.1 was assumed, while the injection borehole was assumed to be entirely filled with grout. This results in an equivalent volume of 0.97 m^3 of injected grout for the magnetic field simulation.

The full model simulation domain was a cube with edges of length 40 m, with the magnetic body located in the centre. This large simulation domain was chosen to allow the magnetic anomaly to decay smoothly to zero at the edge of the domain, thus removing any simulation errors that might be caused by boundary effects.

The background Earth's magnetic field was assumed to be uniform, with components expressed through total intensity ($H_0 = B_0/\mu_0$), and magnetic inclination (θ) and declination angles (α), such that:

$$\begin{aligned} H_{b,x} &= H_0 \cos\theta \sin\alpha, \\ H_{b,y} &= H_0 \cos\theta \cos\alpha, \\ H_{b,x} &= H_0 \sin\theta \end{aligned} \tag{11}$$

The values of inclination and declination chosen for the simulations were based on data from the British Geological Survey for Scotland (BGS, 2015), the magnitude, B_0, was fixed at 50,000 nT, and the inclination and declination angles were taken to be $\theta = -70^\circ$ and $\alpha = -3^\circ$, respectively.

Terrestrial magnetite with a grain size around 5 μm has a typical bulk magnetic susceptibility $\chi = 2$ and remanence $B_{r0} = 100\ \mu_0$ T (Kletetschka et al., 2000). We consider two theoretical grouts with terrestrial magnetite with susceptibilities and remanences of $\chi = 0.05$ and $B_r = 5 \times 10^{-6}$ T and $\chi = 0.1$ and $B_r = 1 \times 10^{-5}$ T, respectively.

Fig. 3 shows contour plots of the magnetic anomaly, that is the change in the total magnetic field due to magnetization of the magnetic grout induced by the Earth's magnetic field and due to remanent magnetization. Fig. 3(a, b) are contours of the magnetic field anomaly in plan view on a plane 0.25 m above the grouted rock cylinder, (c, d) a plane through the centre, and (e, f) a plane 0.25 m below the grouted rock cylinder. In each plot, the small central circle indicates the extent of the injection borehole and the larger circle indicates the extent of the magnetic grout. Results are only shown for a central 3 m × 3 m area in the centre of the model domain. The magnetic anomaly is clearly visible at all depths in Fig. 3, and the magnitude of the anomaly with the higher susceptibility and remanence values is approximately double that predicted with the lower values. Both above and below the grouted cylinder, a dipole (i.e. a maxima adjacent to a minima in the magnetic field) is predicted; at positions above the grouted rock volume (Fig. 3 (a,c)) the magnetic field anomaly is positive to the South of the magnetic body and negative toward the North. The opposite is true at positions below the grouted rock volume (Fig. 3(e,f)) This is as expected for a magnetised body surveyed on a horizontal plane in the Northern Hemisphere (e.g. Reynolds, 2011).

Based on the numerical prediction in Fig. 3, it may be possible to detect magnetic grout if sufficient magnetic particles can be added to a grout mix to be detectable with existing field magnetometer technologies. The achievable detection distance will depend on the magnitude of the field anomaly i.e. the magnetic properties and total mass of the magnetic additive, and the sensitivity that can be achieved with a commercial field magnetometer. A further consideration will be the magnitude and temporal variability of any background magnetic noise.

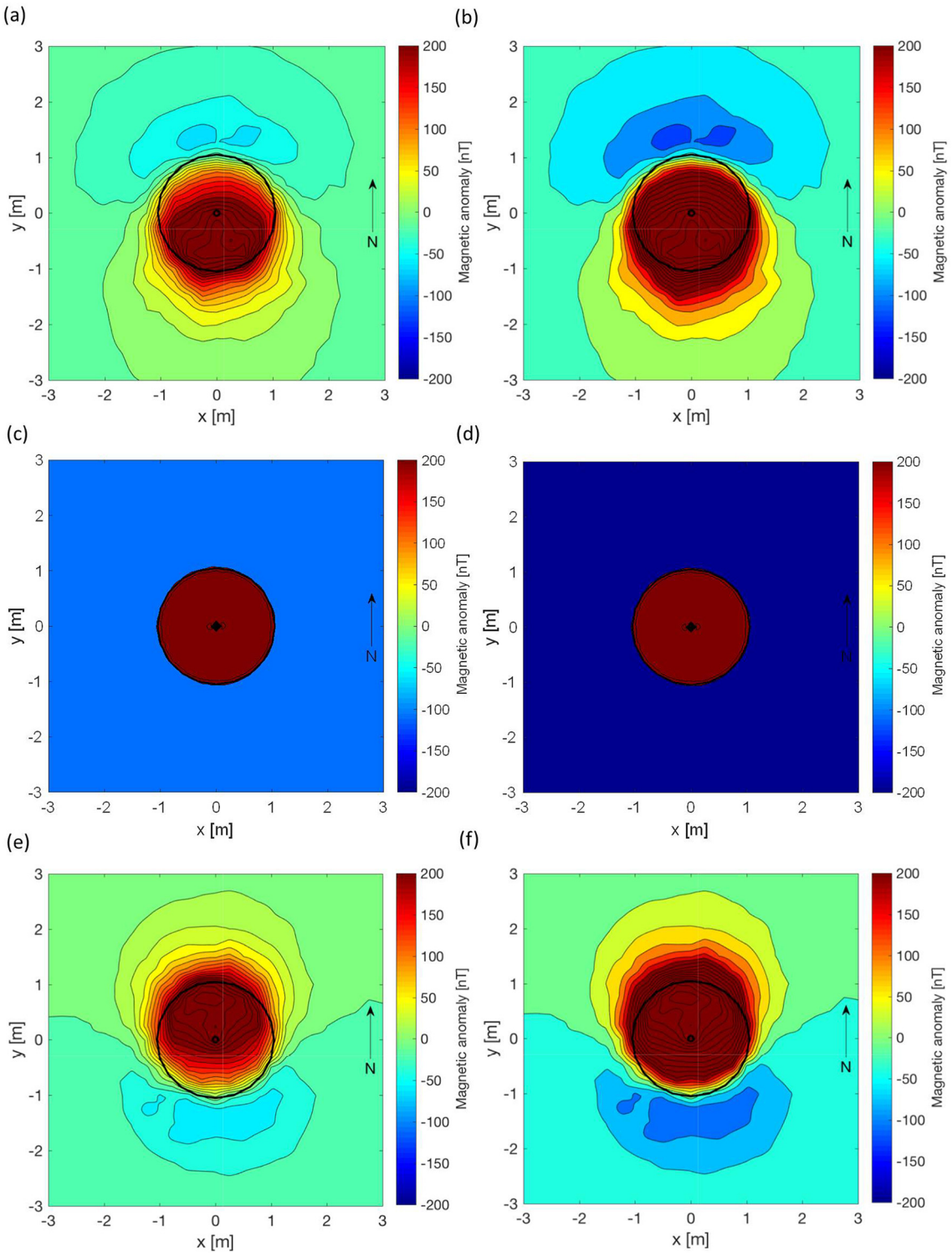

Fig. 3. Contours of the magnetic anomaly given by eq. (9) with (a, c, e) $\chi = 0.05$ and $B_r = 5 \times 10^{-6}$ T, and (b, d, f) $\chi = 0.1$ and $B_r = 1 \times 10^{-5}$ T, on a plane (a, b) 0.25 m above, (c, d) through the centre, and (e, f) 0.25 m below the grouted rock cylinder. In each plot, the small central circle indicates the extent of the injection borehole and the larger circle indicates the extent of the magnetic grout.

3. Experimental methods and materials

In the following sections, the feasibility of a magnetic detection system is explored through the completion of two simple field-based experiments. The first uses surface mapping with a hand-held magnetometer to determine the shape of the magnetic anomaly and demonstrate that burying the grout beneath the ground does not affect magnetic signal attenuation over distance. The second is designed to mimic the feasibility of below-ground grout detection within a borehole monitoring array.

3.1. Magnetic grout preparation

For Field Trial 1, magnetic grout blocks of Ultrafin cement were produced with either 5% or 10% magnetite by mass of cement and a constant water to cement ratio of 0.75, giving a mass of magnetite per unit

Table 1
Dimensions of the large magnetic grout samples.

	Width (cm)	Length (cm)	Depth (cm)	Mass (g)
5% Magnetite				
Rectangle	9.5	22.5	5	1483.55
10% Magnetite				
Rectangle 1	9.5	22.5	4.8	1451.25
Rectangle 2	9.5	22.5	5.2	1492.61
Rectangle 3	9.5	22.5	5	1687.42

volume of grout of 0.039 g cm^{-3} and 0.075 g cm^{-3}, respectively. To ensure that the magnetite was evenly distributed throughout the cement, the magnetite and cement were mixed thoroughly by hand before the addition of water. The cement mixture was decanted into rectangular moulds and left for three days to cure. Table 1 details the dimensions of the magnetic grout blocks produced. The 5% magnetite grout block had a magnetic susceptibility of $\chi = 0.02$, while the 10% magnetite grout blocks had a measured magnetic susceptibility of $\chi = 0.04$.

For Field Trial 2, a single large batch of magnetic grout was produced. This consisted of Ultrafin cement with 10% magnetite by mass of cement, a water to cement ratio of 0.5, with superplasticiser (Glenium 51, 1% of total water) and stabilising agent (GroutAid, 10% of total water) to mimic a realistic commercial grout mix. This gave a mass of magnetite per unit volume of grout of 0.11 g cm^{-3}. To ensure that the magnetite was evenly distributed throughout the cement, the magnetite and cement were mixed thoroughly before the addition of water, and the grout was mixed within a cement mixer until the water had penetrated throughout the dry material. The superplasticiser and stabilising agent were then added to loosen the consistency of the grout. Once the grout was thoroughly mixed, it was evenly distributed between five identical moulds and left for four days to cure. Each mould produced a disc of 0.4 m diameter, 0.07 m height and with a 0.025 m diameter circular hole in the centre. The five discs were stacked to create a single magnetic grout cylinder. The magnetic grout had a measured susceptibility of $\chi = 0.07$. This grout has a larger magnetite content per unit volume and therefore a larger susceptibility than the grout used in Field Trial 1. Furthermore, the magnetite used in Field Trial 2 was from a different source and therefore is likely to have different bulk magnetic properties.

3.2. Magnetic detection

Both field trials were conducted using a Geometrics G-858 MagMapper magnetometer, which is a high-performance caesium vapour total field magnetometer. Optically pumped caesium vapour magnetometers are highly sensitive magnetometers that measure the magnitude of the total magnetic field, with a potential resolution of a few hundred picoteslas and ability to record several measurements per second. The basic principle that allows the device to operate is called optical pumping, where light of a specific wavelength polarizes the caesium atoms by pumping the electrons to a higher energy level where they spontaneously decay to a lower energy level. The atoms are then depolarised by shifting the electrons to their original position using radio wave power of adjustable frequency. The required frequency to depolarise the caesium atoms is proportional to the magnetic field (Smith, 1997).

The G-858 has two caesium vapour total magnetic field sensors, each with a sensitivity of 0.01 nT and specified accuracy of 0.05 nT at 10 Hz. In field trial 1, both sensors were deployed, whereas in field trial 2 only one was used.

3.3. Field trial 1

Field Trial 1 was undertaken in the magnetically quiet environment of Troon Beach, Scotland, UK (55° 53.26′ N, 04° 65.32′ W). The beach environment also allowed for easy burial of the magnetic grout samples to different depths.

In field trial 1, the sensors were positioned vertically with a separation distance of 0.76 m, the lower sensor being 0.50 m above ground level, as shown in 4(a). Fig. 4(b) shows the layout of Field Trial 1. The trial area measured 4.5 m × 5 m with the magnetic grout sample placed at the centre (indicated by the rectangle). Magnetic surveys were taken along transects (indicated with arrows) spaced at 0.5 m intervals walked at a constant pace using a unidirectional approach, with all lines surveyed toward the North. The magnetometer sensors collected data every 0.1 s, taking approximately 40 readings per line.

Each day, a background magnetic survey of the trial area was taken as a baseline. Magnetic surveys were then carried out with the magnetic grout blocks placed in the centre of the trial area. The following configurations of magnetic grout blocks at the surface were used: a single rectangular block with 5% magnetite, a single rectangular block with 10% magnetite (Table 1, Rectangle 2), three rectangular blocks with 10% magnetite orientated as shown in Fig. 4(c), and three rectangular blocks with 10% magnetite stacked with the long-axis orientated North-South.

Finally, the three rectangular blocks with 10% magnetite orientated as shown in Fig. 4(c) were buried at five different depths from the ground surface as measured from the top of the blocks: 0 m (so the top of the sample was level with the ground surface), 0.065 m, 0.15 m, 0.30 m, and 0.40 m depth.

3.4. Field trial 2

Field Trial 2 was also conducted at Troon Beach and was designed to mimic data acquisition from a borehole injection test. The magnetic

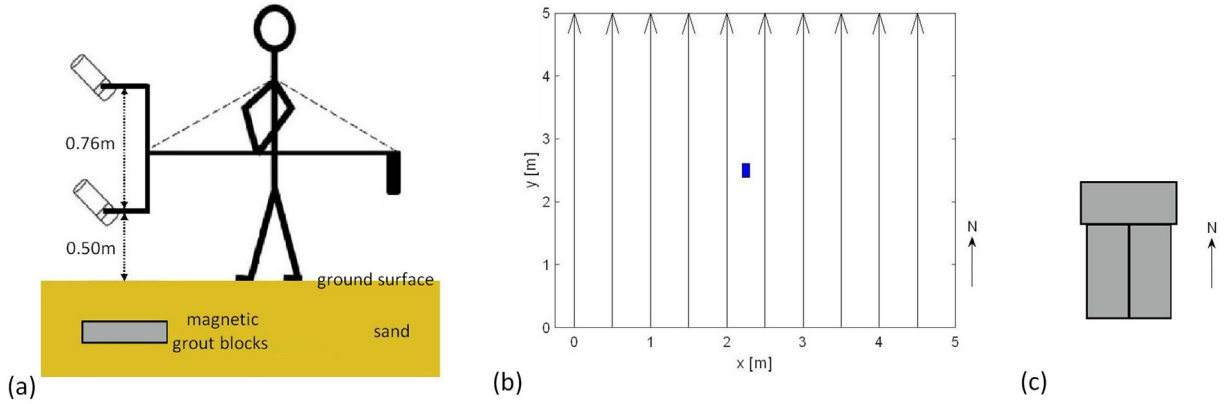

Fig. 4. Diagram of (a) the arrangement of the magnetometer sensors for trial 1; (b) the layout of trial 1; (c) the orientation of the rectangular blocks in the flat configuration. In (b), the rectangle represents the magnetic grout, and the arrows indicate the transects along which magnetic field measurements were taken, evenly spaced at 0.5 m intervals.

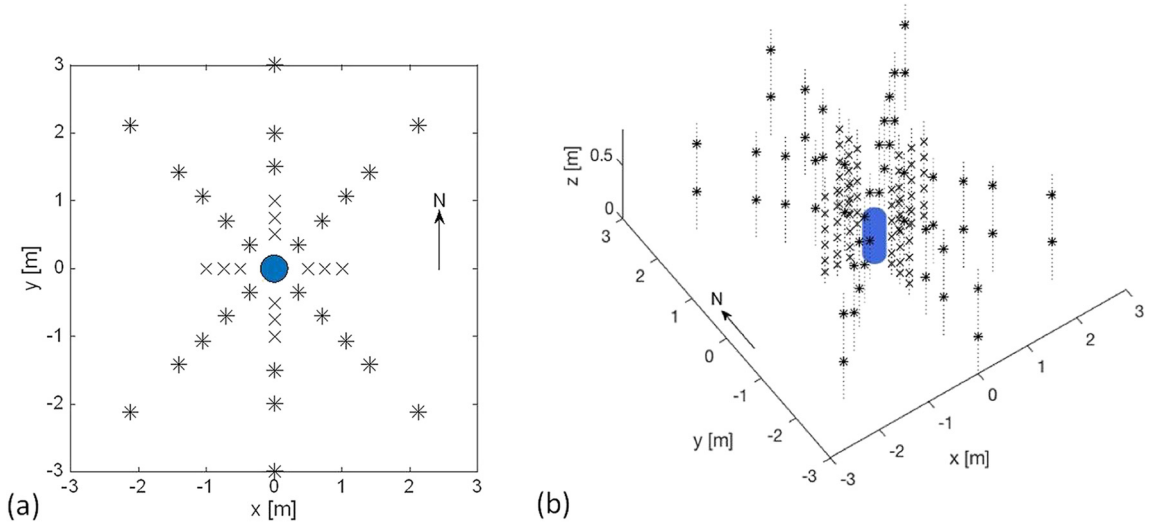

Fig. 5. (a) Plan view and (b) 3D view of the layout of Field Trial 2. In (a) the circle, and in (b) the cylinder represent the magnetic grout. Magnetometer readings were taken at heights above ground level of 0.1 m, 0.2 m, 0.35 m, 0.5 m, 0.65 m, 0.8 m at locations indicated by crosses, and at heights above ground level of 0.35 m and 0.8 m at locations indicated by asterisks.

grout discs were stacked centrally on the ground surface so the top of the cylinder was 0.35 m above ground level. Magnetic field data were collected at multiple heights above ground for several monitoring locations designed to mimic a borehole monitoring array. Fig. 5 shows the layout of Field Trial 2.

For each sampling location, magnetic field measurements were recorded at differing heights above ground by fixing both magnetometer sensors to a vertical wooden pole with a marked scale, so that each sensor could be accurately located. During the trial the magnetometer sensors were sited so that the top of the sensor holder was aligned with the marked vertical height position on the pole, and the sensors were orientated to point North. To minimise location errors, a Trimble S6 Total Station was used to survey the different pole positions and to ensure that the pole was always vertical. Magnetometer readings were taken at heights above ground level of 0.1 m, 0.2 m, 0.35 m, 0.5 m, 0.65 m, 0.8 m at locations indicated by crosses, and at heights above ground level of 0.35 m and 0.8 m at locations indicated by asterisks in Fig. 5.

3.5. Magnetic field data processing

In general, the Earth's magnetic field is neither spatially nor temporally constant. Further, variations in the magnetic properties of soils and rocks can cause significant spatial variations in the recorded background magnetic field. Fig. 6 plots a sample of the background magnetic field from Field Trial 1 at Troon, showing a variation of approximately 50 nT over the surveyed region.

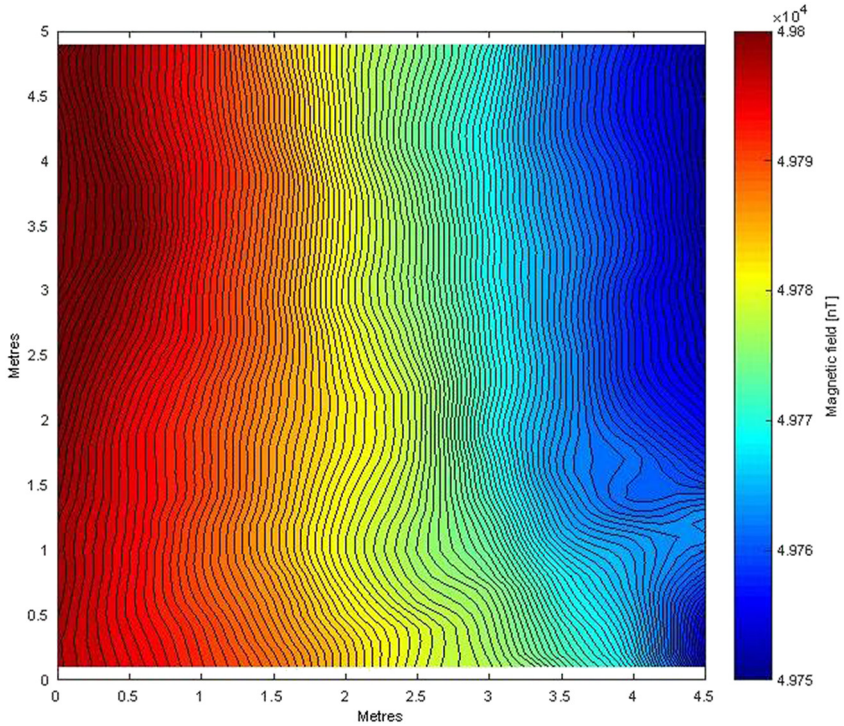

Fig. 6. Contour plot of the background magnetic field.

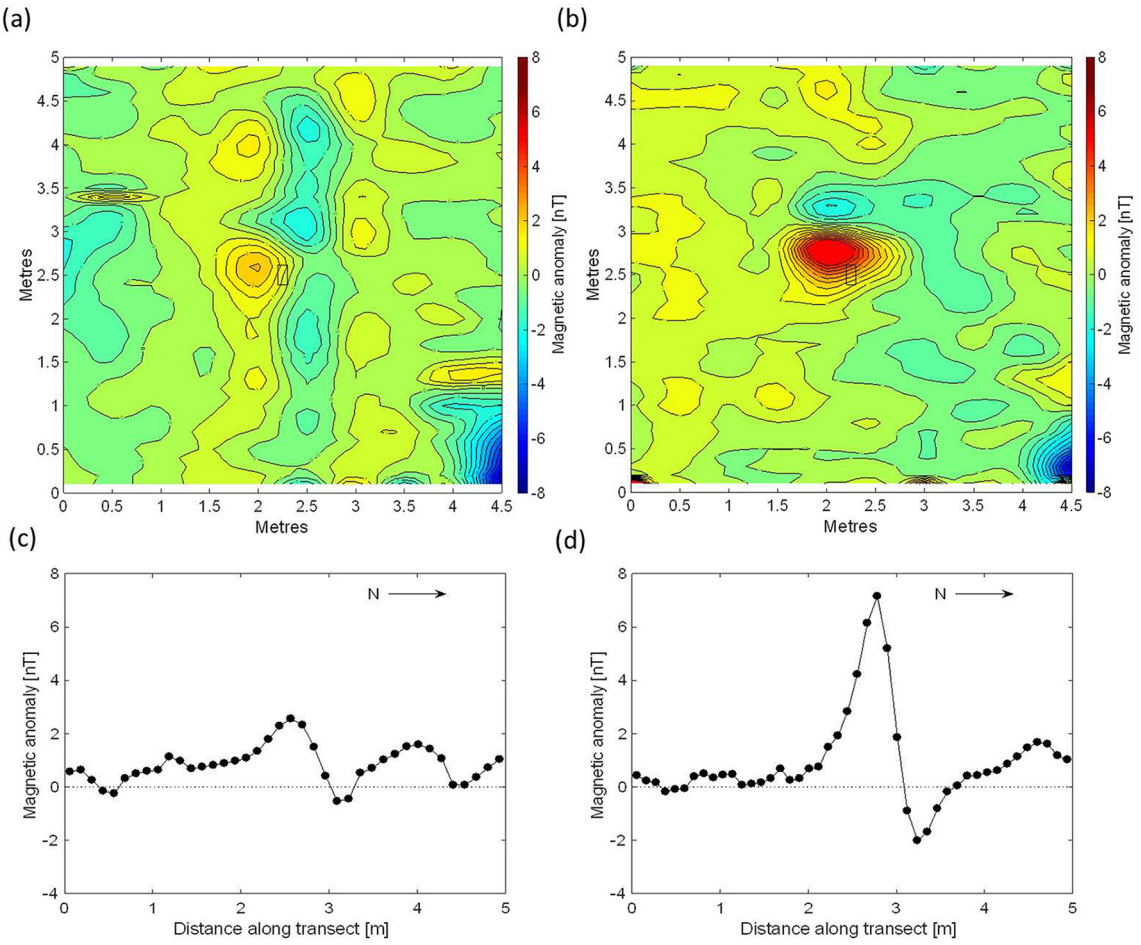

Fig. 7. Contour plot of the magnetic anomaly of one rectangular block with (a) 5% magnetite, and (b) 10% magnetite; plot of the magnetic anomaly along the 2 m survey line for (c) 5% magnetite, and (d) 10% magnetite.

As a result of the variability in the background field, for both field trials, a baseline magnetic survey was conducted on each day. The magnetic anomaly due to the emplaced magnetic grout blocks was then determined by subtracting the baseline magnetic field data from the magnetic field recorded once the blocks were in place.

In Field Trial 1, data from the lower sensor was used, as discussed above, to determine the magnetic anomaly field by removing the baseline magnetic field. However, in Field Trial 1 the horizontal and vertical locations of the sensors were not accurately known as it was a handheld walkover survey. The upper sensor, which was much less affected by the presence of the magnetic grout blocks, was used to estimate variation in the background field, due to changes in the positioning of the sensors between surveys. This estimate was then used to correct the magnetic anomaly field derived from the lower sensor.

In order to contour the results from Field Trial 2, additional measurement points at a distance of 4 m from the magnetic discs were added to each dataset. These additional points were set to have a magnetic anomaly of 0 nT since theoretically the magnetic anomaly must tend to zero at some distance from the discs. Each dataset was interpolated onto a regular grid using the function *griddata* with natural interpolation in MATLAB, and then contoured.

4. Results

4.1. Field trial 1 results

Fig. 7 shows contour plots of the magnetic field anomaly for a single rectangular block with 5% magnetite and a single rectangular block with 10% magnetite, alongside graphs showing the magnitude of the magnetic anomaly on the walkover transect line (Fig. 4a) that contained the maximum anomaly value (the 2 m transect line in this case). Comparing the contour maps and plots in Fig. 7 shows that the magnetic anomalies produced with 5% and 10% magnetite are similar in shape. However, doubling the mass of magnetite within the sample produces a magnetic anomaly that is more than twice the size; with the peak recorded value rising from 2.55 nT to 7.15 nT (cf. Fig. 7c and d).

Fig. 8 shows contour plots (a, b) and cross-sections (c, d) of the magnetic field anomalies recorded using three rectangular blocks, each with 10% magnetite, stacked in two different configurations: a flat configuration orientated as shown in Fig. 4(c) (Fig. 8a and c), and a stacked configuration with the long-axis orientated North-South (Fig. 8b and d). For each configuration, the cross section is plotted for the walkover transect line that contains the maximum value of the anomaly. For both configurations, the magnetic anomaly is easily identified, with a dipole visible orientated along the North East-South West axis in the flat configuration (Fig. 8a), and oriented along the North-South axis in the stacked configuration (Fig. 8b). The maximum recorded magnetic anomaly for the flat and stacked configurations are 20.03 nT (Fig. 8c) and 8.81 nT (Fig. 8d) respectively. Hence, the flat configuration records a greater peak anomaly.

Fig. 9 shows contour plots of the magnetic field anomaly for the same three rectangular bricks (in the flat configuration) placed at six different vertical distances with respect to the ground surface, as measured from the top of the blocks: −0.05 m with base of the bricks at the ground surface as before; 0 m i.e. buried such that the top of the sample was level with the ground surface; four other burial depths for

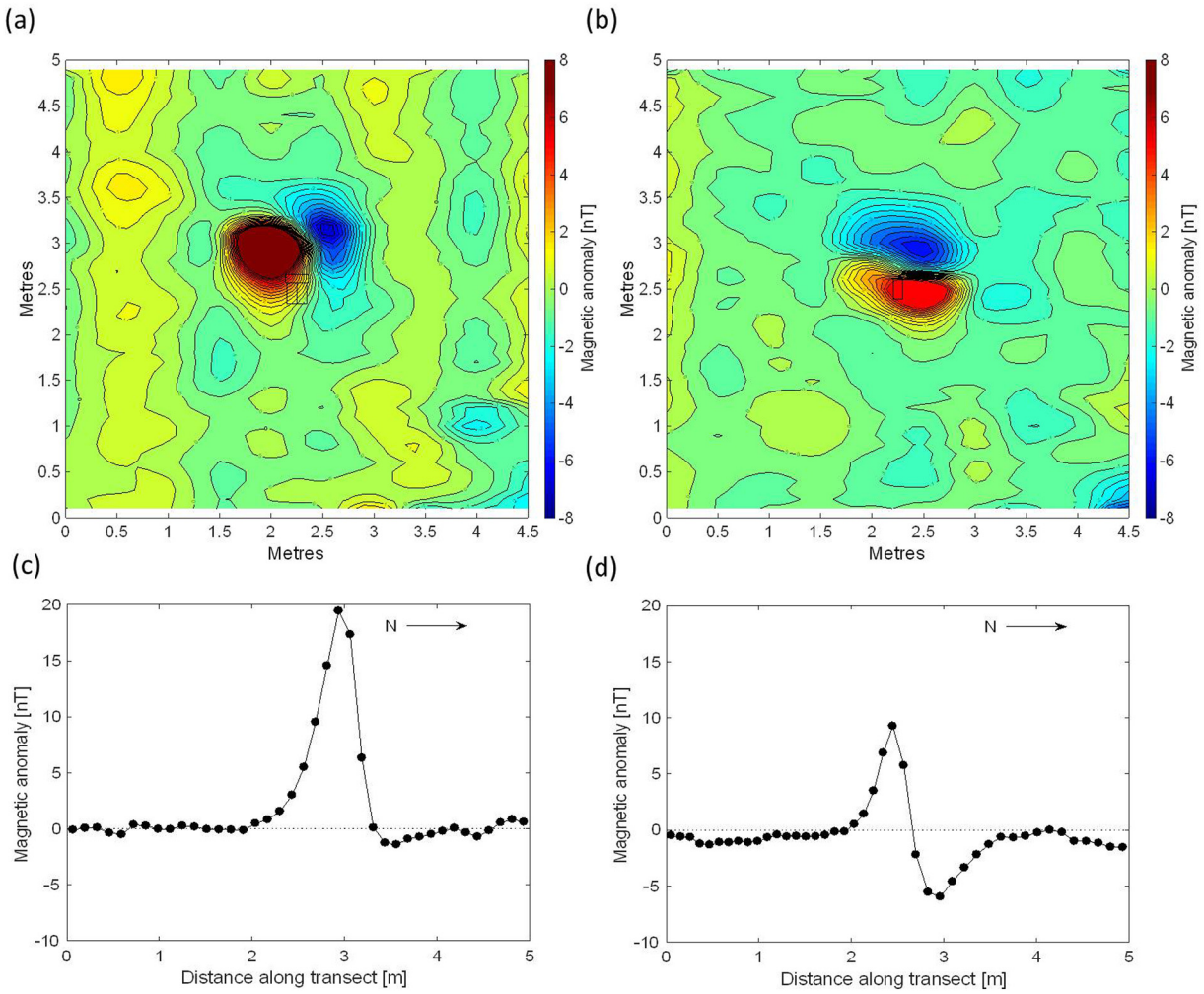

Fig. 8. Contour plot of the magnetic anomaly for 3 rectangular blocks each with 10% magnetite in a (a) flat configuration, and (b) stacked configuration; plot of the magnetic anomaly along (c) the 2 m survey line for the flat configuration, and (d) the 2.5 m survey line for the stacked configuration.

which the top of the brick was buried at 0.065 m, 0.15 m, 0.30 m, and 0.40 m beneath the ground surface respectively. Fig. 10 shows the corresponding cross-sections, for each depth for the walkover transect that contains the peak magnetic anomaly. From Figs. 9 and 10 it can be seen that increasing the distance from the lower magnetometer sensor reduces the size of the magnetic anomaly. The shape of the anomaly also changes from being relatively rounded to being elongated for the samples located at a greater distance (Fig. 9). This change in shape is also visible in Fig. 10 with narrow peaks present when the magnetic grout rectangles are located closer to the magnetometer, and wider peaks when they are located further away. While a dipole is visible orientated along the North East-South West axis when the rectangular blocks are at the surface (Fig. 9a), dipoles are not clearly present when the distance from the lower magnetometer sensor is increased.

4.2. Field trial 2 results

Fig. 11 shows contour plots of the magnetic anomaly at six different magnetometer sensor heights above ground level. For readings taken below the top of the magnetic discs (Fig. 11a, b), i.e., below 0.35 m, the magnetic anomaly is negative at all measurement locations, with the largest negative anomalies recorded at the measurement locations closest to the sample in a southerly direction; −5871 nT at 0.1 m from the sample and −405 nT at 0.2 m.

When surveying at a position level with the top of the magnetic discs (Fig. 11c), the magnetic anomaly remains negative at all measurement locations, with the largest negative anomaly being recorded at the closest measurement location to the north of the sample (−771 nT).

When surveying at positions above the magnetic discs (Fig. 11d–f), i.e., above 0.35 m, a magnetic dipole with the positive lobe orientated to the south is apparent. At all heights above the sample, the largest positive anomaly is recorded at the closest measurement location to the south of the sample. As distance from the sample increases (i.e. the height increases) the magnitude of the peak anomaly decreases (292 nT at 0.5 m; 211 nT at 0.65 m; 149 nT at 0.8 m). The largest negative anomaly is recorded at the closest measurement location to the north of the sample, again, this decreases as the vertical height, and hence distance from the sample, increases (−65 nT at 0.5 m; −20 nT at 0.65 m; −3.5 nT at 0.8 m).

4.3. Discussion of the field trials

Both field trials clearly show that the magnetic grout samples produce a magnetic anomaly that is detectable using a commercially available field magnetometer. The size and shape of this magnetic anomaly is dependent on a number of factors, including the percentage of magnetite in the grout mix, the shape of the sample, and the vertical and horizontal distance of the sensors from the sample.

From Field Trial 1, doubling the mass of magnetite in a single rectangular block more than doubles the magnitude of the magnetic anomaly (Fig. 7). This is likely an error due to inaccuracies in the locations of the walkover transect lines with respect to the locations of the bricks.

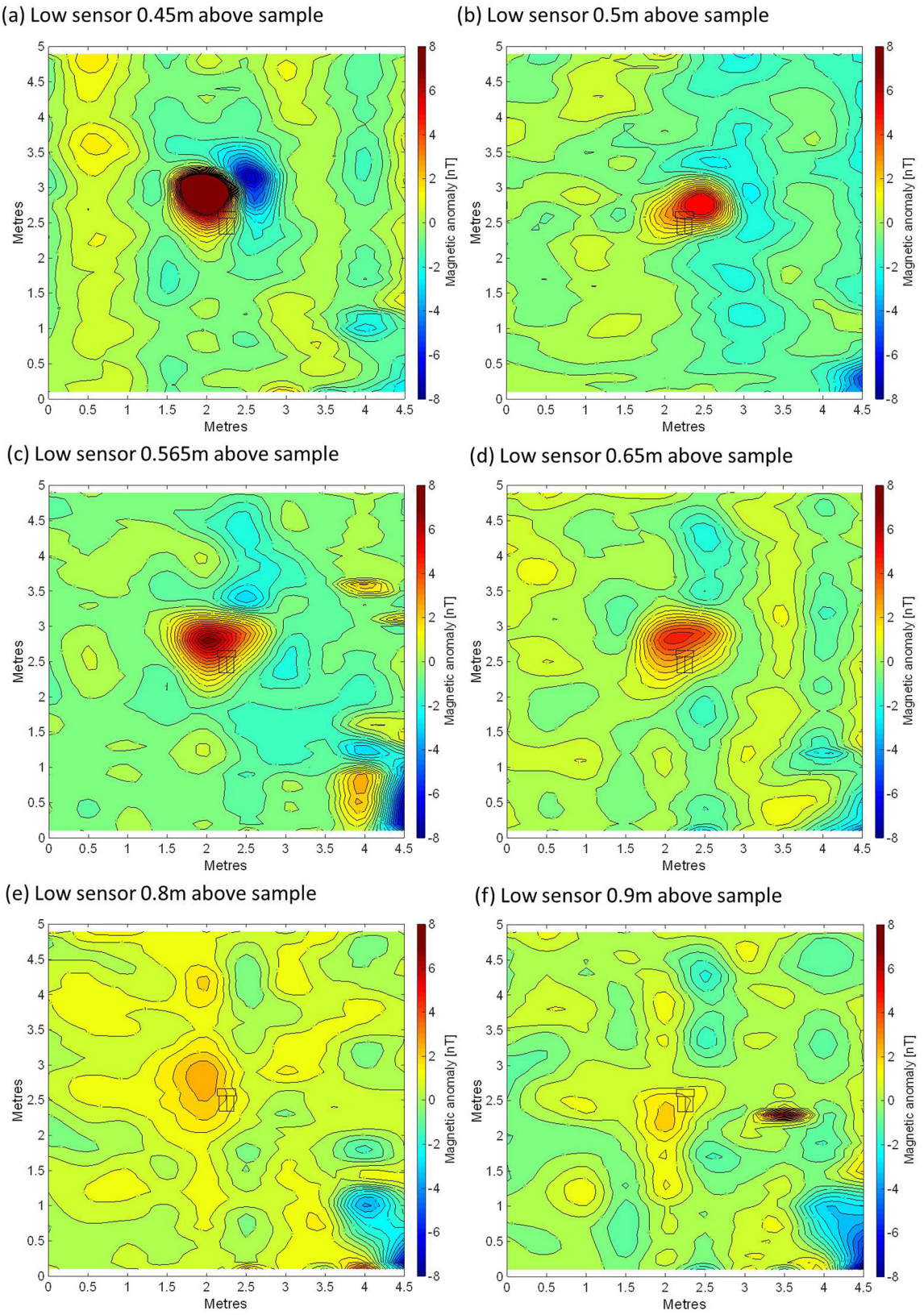

Fig. 9. Contour plots of the magnetic anomaly for the flat configuration of 3 rectangular blocks each with 10% magnetite (a) placed on the surface; and buried at five different depths from the ground surface as measured from the top of the blocks: (b) 0 m (so the top of the sample was level with the ground surface), (c) 0.065 m, (d) 0.15 m, (e) 0.30 m, and (f) 0.40 m.

Increasing the number of rectangular blocks from one to three also increased the magnitude of the magnetic anomaly, but the amount of increase depended on the configuration of the blocks: when compared to results for a single block, the flat configuration produced a magnetic anomaly almost three times as large, whereas the stacked configuration only produced a slight increase from 7.15 nT to 8.81 nT (Fig. 8). Again, this difference in maximum anomalies may be due to errors in the magnetometer location: for the stacked bricks the magnetic anomaly will be

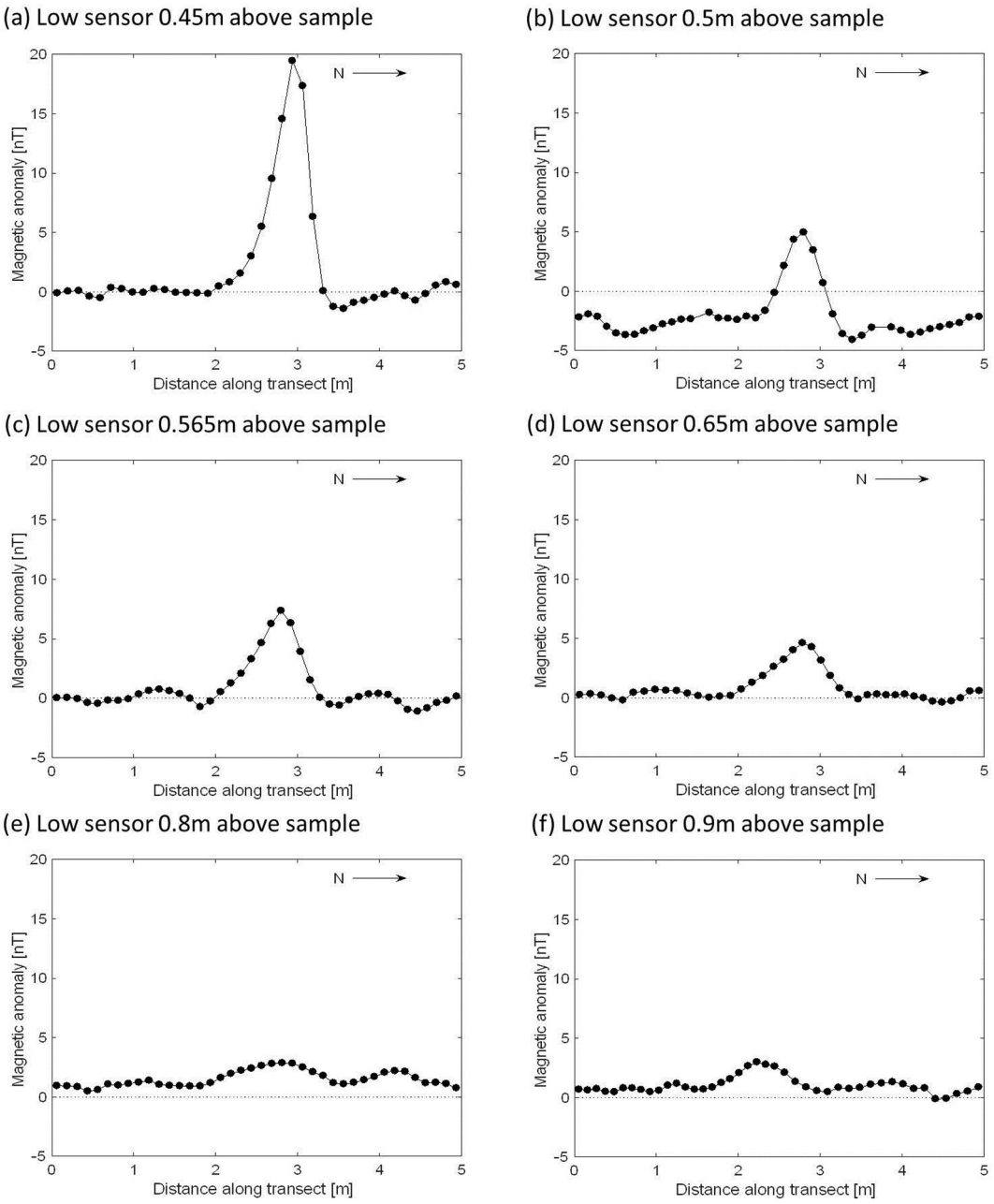

Fig. 10. Plots of the magnetic anomaly along the survey line with the maximum anomaly for the flat configuration (a) placed on the surface; and buried at five different depths from the ground surface as measured from the top of the blocks: (b) 0 m (so the top of the sample was level with the ground surface), (c) 0.065 m, (d) 0.15 m, (e) 0.30 m, and (f) 0.40 m.

smaller in diameter and, therefore, it would be easier to miss the peak value during the walkover survey with 0.5 m gaps between the survey lines.

Field Trial 1 also demonstrated that increasing the distance between the grout sample and the lower magnetometer sensor generally decreased the size and width of the magnetic anomaly (Fig. 10), but the magnetic anomaly was still detectable 0.9 m above the grout sample.

In Field Trial 2, the locations for recording the magnetic field were sparse to mimic the data that could conceivably be collected from monitoring boreholes. This use of fixed monitoring points, however, allowed the magnetometer location to be determined with far greater accuracy through the use of surveying equipment. Field Trial 2 showed that at vertical heights within the vertical range of the magnetic discs, i.e. at 0.1 m and 0.2 m above ground, the magnetic anomaly is negative at all measurement locations. Whereas, for vertical heights above the magnetic discs, i.e. at 0.5 m, 0.65 m, and 0.8 m, the magnetic anomaly takes the form of a dipole with the positive lobe orientated toward the south.

Field Trial 2 also showed that as the horizontal distance from the magnetic grout increases, the magnetic anomaly decreased for all vertical heights with respect to the magnetic discs. In this trial, the maximum horizontal detection distance was between 1.5 m and 2 m.

5. A comparison of the theoretical and numerical model with the field observations

To simulate the two field trials, the numerical model domain was chosen to be a cube with edges of length 40 m, with the grout blocks located in the centre of the domain in order to minimise boundary effects. Based on data provided by the British Geological Survey (BGS, 2015), for both field trials the inclination and declination were

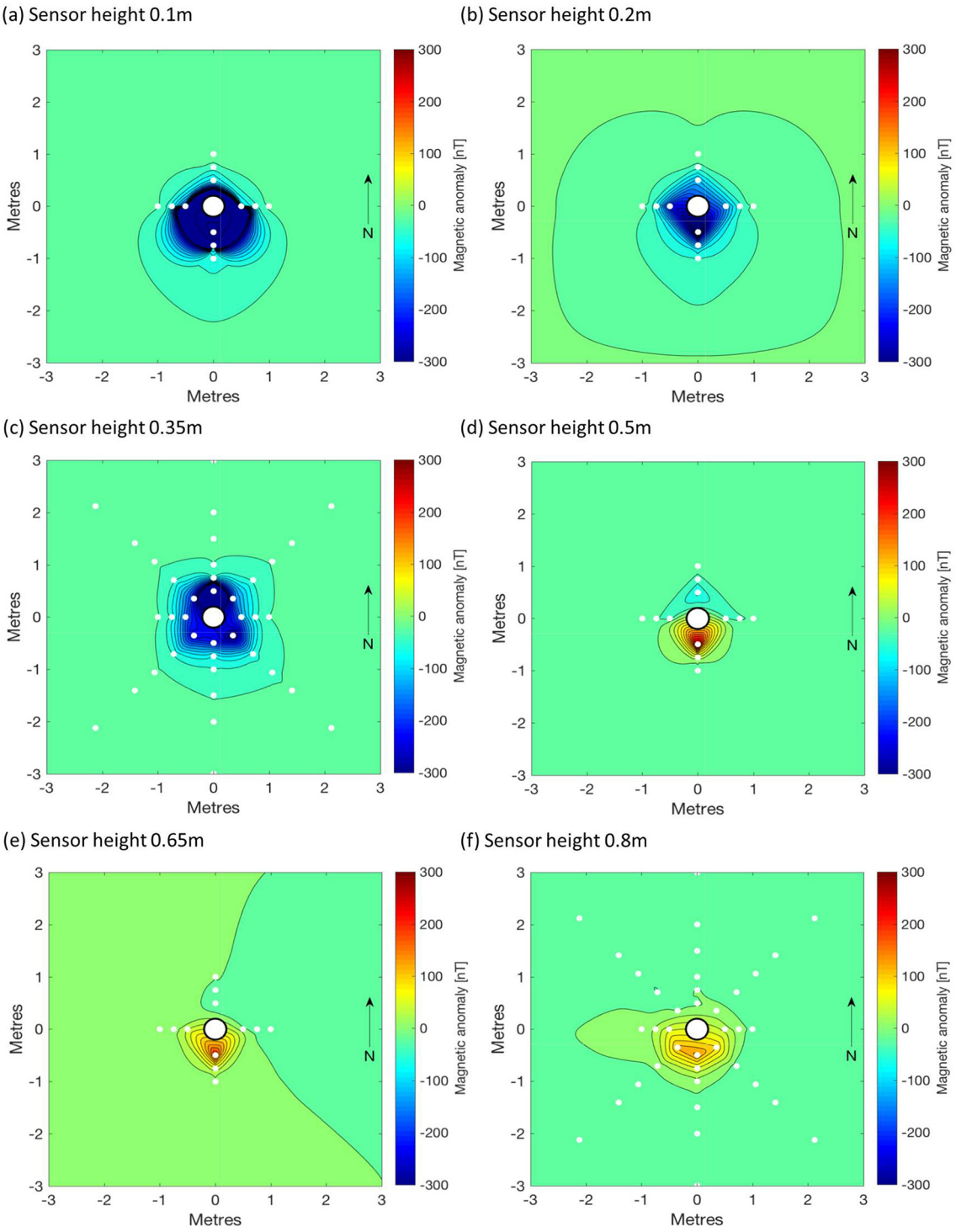

Fig. 11. Contour plots of the magnetic anomaly with the magnetometer sensor at (a) 0.1 m, (b) 0.2 m, (c) 0.35 m, (d) 0.5 m, (e) 0.65 m, and (f) 0.8 m above ground level. The white circle in the centre represents the location of the magnetic grout, and the white dots represent the measurement locations.

approximately $\theta = -69.5^{\circ}$ and $\alpha = -3.1^{\circ}$, respectively. The magnitude of the magnetic flux density ($B_0 = \mu_0 H_0$) was 49,800 nT.

For Field Trial 1, we compare the detected and modelled magnetic anomaly produced by three rectangular blocks, each with 10% magnetite, in the stacked configuration with their long-axis orientated North-South. The model used magnetic parameter values of $\chi = 0.04$ and $B_{r0} = 0$ nT. To allow a comparison of the detected and modelled anomalies, the modelled anomaly was calculated using the same process as used for the field data in Field Trial 1 (Section 3.5). Fig. 12(a) shows the modelled magnetic anomaly and, to aid the reader in comparing the two results, Fig. 12(b) reproduces the detected anomaly as shown in Fig. 8(b). A direct comparison of results between the model and the field data is not possible for Field Trial 1, due to the poor control on sensor location in the field. However, general understanding of the orientation, magnitude and shape of the magnetic field produced by the magnetic grout blocks can be confirmed. Comparing Fig. 12(a) and (b), we see that the general shape of the magnetic anomaly is reproduced by the model, with a positive anomaly located over the disks and to the south and a negative anomaly toward the north. The predicted negative anomaly in the numerical

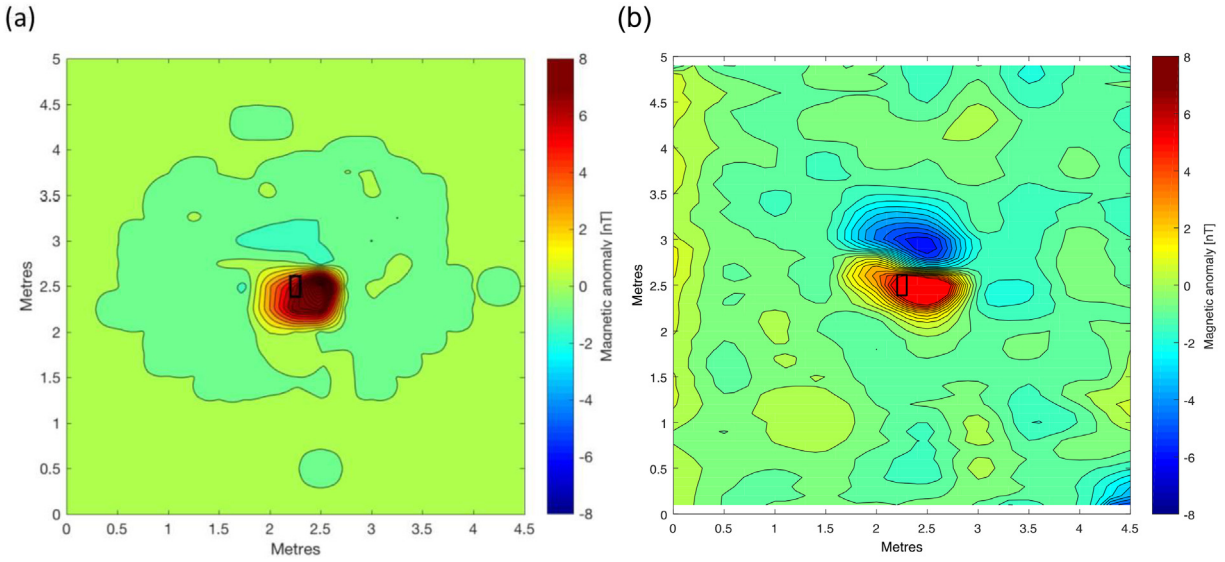

Fig. 12. Contour plots of the (a) modelled and (b) detected magnetic anomaly produced by three rectangular blocks, each with 10% magnetite, in the stacked configuration with the long-axis orientated North-South. The detected magnetic anomaly in (b) is reproduced from Fig. 8(b).

simulation is not as large as that observed in the field, while the predicted positive anomaly in the numerical simulation is slightly larger. This discrepancy is likely to be a combination of neglecting the remnant magnetisation in the model as well as location errors in calculating the detected anomaly.

For the simulation of Field Trial 2, in which the sensor locations were accurately known, model calibration was performed to give as good a fit as possible to the field data. It was found that to fit the field data, a remnant magnetic flux density was required, without which the peak magnetic field values were too small. This magnetic remanence was

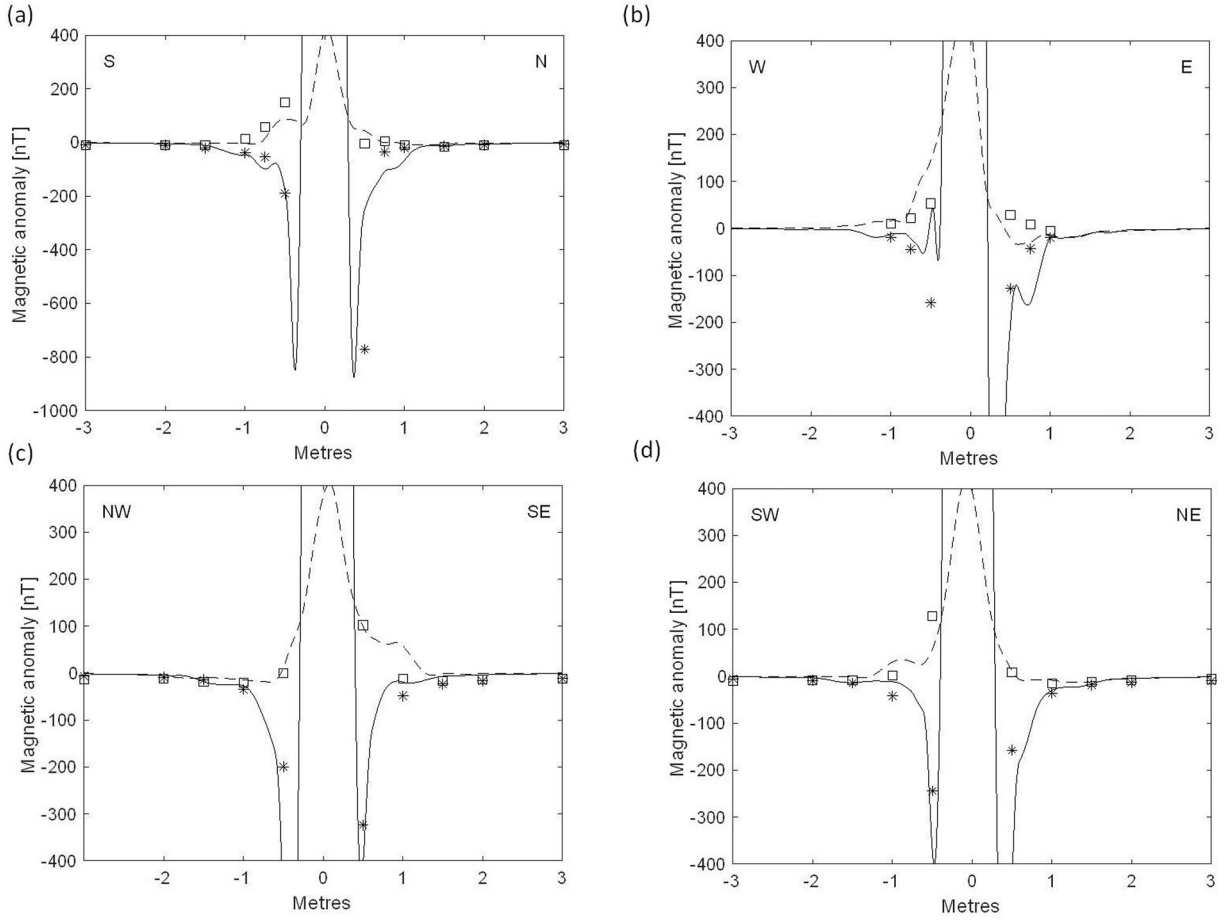

Fig. 13. Comparison of the measured and modelled magnetic anomaly. In each plot the asterisks and squares represent the measured magnetic anomaly at 0.35 m and 0.8 m, respectively, while the solid and dashed lines represent the modelled magnetic anomaly at 0.35 m and 0.8 m, respectively.

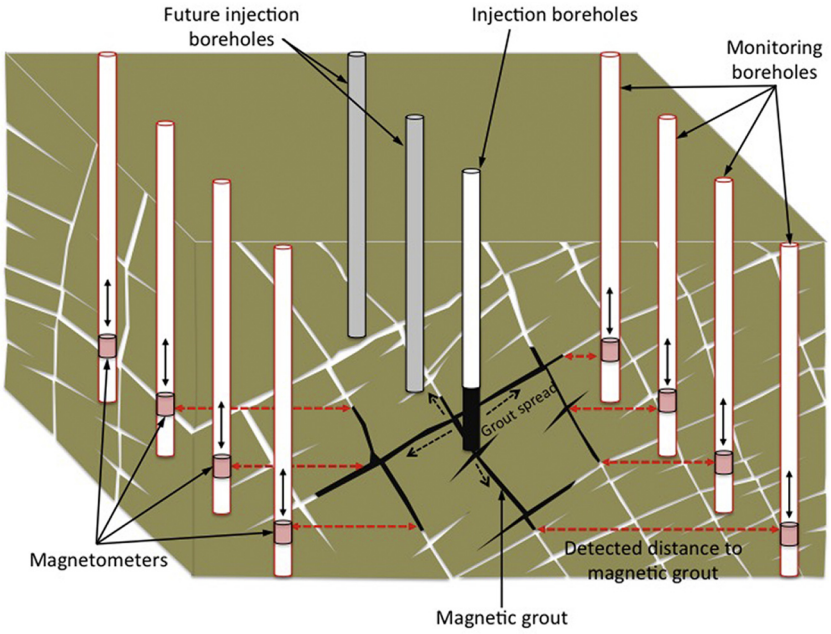

Fig. 14. Deployment of magnetic grout technique during a commercial grouting operation.

best fit with a remanent magnetic field magnitude of $B_{r0} = 1 \times 10^{-5}$ T and a principle orientation of the remanent field that aligned with the background geomagnetic field. Recall from Section 2.3 that terrestrial magnetite with a grain size around 5 μm has a typical bulk remanence $B_{r0} = 100\mu_0$ T (Kletetschka et al., 2000). In Field Trial 2, the grout contained 0.11 g cm^{-3} magnetite, which gives a predicted remanence of $B_{r0} = 1.4 \times 10^{-5}$ T. The need to include remanence within the model implies that the magnetite mineral powder added to the cement has some small permanent magnetism, as well as being magnetically susceptible.

Fig. 13 shows a comparison of the calibrated model simulation with the field observations for Field Trial 2 where the asterisks and squares represent the measured magnetic anomaly at 0.35 m and 0.8 m, respectively, while the solid and dashed lines represent the modelled magnetic anomaly at 0.35 m and 0.8 m, respectively. At all orientations, there is reasonably good agreement between the measured and the modelled anomaly.

6. Discussion

The theoretical sensitivity of commercial laboratory and field magnetometers varies from micro Teslas to pico Teslas, hence, based on the results of these trials, magnetic grout could be detectable over very large distances. However, the spatial and temporal variations that were observed in the background magnetic field readings during the field trial period would suggest that, in practice, magnetic anomalies less than 1 nT may not be clearly distinguishable. Detection distances depend on the volume of grout injected, the mass of magnetic material added and its magnetic properties. For the 43 l of 10% magnetite grout used in field trial 2, an anomaly of 1 nT is predicted to occur at a distance of 3.5 m from the grout front; doubling the percentage of magnetite would double this predicted detection distance to 7 m.

To use this concept to determine the shape and location of grouted rock volumes at depth requires further research effort. Fig. 14 shows a possible configuration for the deployment of magnetic grout during a commercial grouting operation. By recording the magnetic field throughout the full depth of each monitoring borehole, measurements would be acquired similar to those presented in Fig. 7d (but in the vertical) as the sensors move down each borehole past the magnetic grout. The magnitude of the peaks and troughs in each vertical profile will be governed by the distance between each individual monitoring borehole and the magnetic grout front at that depth, whereas the direction of the magnetic field will be related to the shape of the grouted rock volume. To automate determination of the shape and location of the magnetic grout, from magnetic anomaly data, will require the development of inversion and optimization software.

7. Conclusions

Grouted barrier construction is limited by the current inability to determine the distribution of grout post-injection, making verification of grout curtain geometry highly complex. This leads to a high level of grout redundancy and conservatism, coupled with extensive post-construction performance validation.

In this paper, the feasibility of a detectable permeation grouting system is tested based on the addition of magnetic materials to cementitious grouts. First, a numerical model was developed to demonstrate conceptual feasibility of the system. The model is verified via comparison to a simple analytical solution for a magnetic sphere. Once verified, it was applied to demonstrate the size of the magnetic anomaly that could be generated via borehole injection of a magnetically susceptible cement grout. Two simple field trials were then conducted to validate this magnetically detectable grouting concept. The first field trial used a walkover survey that allowed 2D mapping of the magnetic signal, both for buried magnetic grout samples and samples placed at the surface. The second field trial was designed to mimic the magnetic field measurements from a borehole monitoring array and used a single central magnetic grout block (representing the grout injection point) and a small number of known monitoring points surveyed to have accurate locations.

Results of the two field trials show that the magnetic cement is detectable, even when the background magnetic noise within the surrounding soils/rocks is significant. The orientation and shapes of the 3D magnetic field anomalies observed within the field trials compare well with those predicted by the numerical model. Using data from Field Trial 2, the numerical model is calibrated and a good agreement between the measured and modelled anomaly is obtained. The model simulations demonstrate that monitoring distances of several meters are likely achievable by a magnetically-based detectable grouting system. Finally, a concept for commercial deployment of the magnetically

detectable grout is proposed. In summary, our findings suggest that magnetically detectable grout has the potential both to increase confidence in the integrity of commercial grout operations and to reduce the inefficiencies currently present in the grouting industry; by enabling grout detection, the door can be opened to in-situ real-time optimisation of grout campaigns.

Acknowledgements

The research was guided by helpful discussions with Mr. Alasdair Henderson, People and Culture Director, BAM Nuttall Ltd.

Funding

Fieldwork was funded by a UK Engineering and Physical Sciences Research Council Doctoral Training Award Grants EP/K503174/1 and EP/J500550/1. Model development was funded via Innovate UK Project no. 102066.

All data underpinning this publication are openly available from the University of Strathclyde KnowledgeBase at http://dx.doi.org/10.15129/70026379-a0c8-428f-a012-51f4bbdf5583.

The research presented in this paper is covered by European Patent No. EP3137688 (patent granted).

References

Brantberger, M., Stille, H., Eriksson, M., 2000. Controlling grout spreading in tunnel grouting analyses and development of the GIN-method. Tunnel. Underground Space Technol. 15 (4), 343–352.

British Geological Survey, World Magnetic Model 2015 Calculator, http://geomag.bgs.ac.uk/data_service/models_compass/wmm_calc.html.

Chen, Y., Nishiyama, T., Terada, M., Iwamoto, Y., 2000. A fluorescent approach to the identification of grout injected into fissures and pore spaces. Eng. Geol. 56, 395–401.

El Tani, M., 2012. Grouting rock fractures with cement grout. Rock Mech. Rock. Eng. 45 (4), 547–561.

Griffiths, D.J., 1999. Introduction to Electrodynamics. 3rd edition. Prentice Hall, New Jersey.

Hecht, F., 2012. New development in FreeFem++. J. Numer. Math. 20, 251–265.

Henderson, A.E., Robertson, I.A., Whitfield, J.M., Garrard, G.F.G., Swannell, N.G., Fisch, H., 2008. A new method for real-time monitoring of grout spread through fractured rocks. MRS Proc. **1107**.

Kletetschka, G., Wasilewski, P.J., Taylor, P.T., 2000. Hematite vs. magnetite as the signature for planetary magnetic anomalies? Phys. Earth Planet. Inter. **119**, 259–267.

Li, S., Liu, R., Zhang, Q., 2016. Protection against water or mud inrush in tunnels by grouting: a review. J. Rock Mech. Geotech. Eng. 8 (5), 753–766.

Lombardi, G., 1996. Selecting the grouting intensity. Int. J. Hydropower Dams 4, 62–66.

Majer, E.L., 1989. The application of high frequency seismic monitoring methods for the mapping of grout injections. Int. J. Rock Mech. Min. Sci. Geomech. Abstr. 26, 249–256.

Meier, L., Hoffmann, A.G., 1999. Mine shaft stabilization using compaction grouting. Geo-Engineering for Underground Facilities. Reston, VA, American Society of Civil Engineers.

Rafi, R., Stille, H., 2015. Applicability of using GIN method, by considering theoretical approach of grouting design. Geotech. Geol. Eng. 33, 1431–1448.

Rastegarnia, A., Sohrabibidar, A., Bagheri, V., 2017. Assessment of relationship between grouted values and calculated values in the Bazoft dam site. Geotech. Geol. Eng. 35 (4), 1299–1310.

Reynolds, J.M., 2011. An introduction to Applied and Environmental Geophysics. 2nd Edition. Wiley-Blackwell, p. 710 (ISBN 978-0-471-48535-3).

Smith, K., 1997. Cesium optically pumped magnetometers: basic theory of operation. Technical Report M-TR91. Geometrics.

Tsuda, H., Walker, C., Shinkai, F., Kishi, H., Yui, M., 2012. Development of a grout database for geological disposal of high-level radioactive waste. J. Nucl. Sci. Technol. 49 (11), 1110–1113.

Zhang, F., Xie, X., Huang, H., 2010. Application of ground penetrating radar in grouting evaluation for shield tunnel construction. Tunn. Undergr. Space Technol. 25, 99–107.